# Multidimensional Spectral Fingerprints of a New Family of Coherent Analytical Spectroscopies

Nathan A. Neff-Mallon, and John C. Wright<sup>1</sup>

Department of Chemistry, University of Wisconsin-Madison, Madison, WI 53706

#### **Abstract**

Triply Resonant Sum Frequency (TRSF) and Doubly Vibrationally Enhanced (DOVE) spectroscopies are examples of a recently developed family of Coherent Multidimensional Spectroscopies (CMDS) that are analogous to multidimensional NMR and current analytical spectroscopies. CMDS methods are particularly promising for analytical applications because their inherent selectivity makes them applicable to complex samples. Like NMR, they are based on creating quantum mechanical superposition states that are fully coherent and lack intermediate quantum state populations that cause quenching or other relaxation effects. Instead of the nuclear spin states of NMR, their multidimensional spectral fingerprints result from creating quantum mechanical mixtures of vibrational and electronic states. Vibrational states provide spectral selectivity and electronic states provide large signal enhancements. This paper presents the first electronically resonant DOVE spectra and demonstrates the capabilities for analytical chemistry applications by comparing electronically resonant TRSF and DOVE spectra with each other and with infrared absorption and resonance Raman spectra using a Styryl 9M dye as a model system. The methods each use two infrared absorption transitions and a resonant Raman transition to create a coherent output beam but they differ in how they access the vibrational and electronic states and the frequency of their output signal. Just as FTIR, UV-VIS, Raman, and Resonance Raman are complimentary methods, so also are TRSF and DOVE methods complementary to coherent Raman methods such as Coherent Anti-Stokes Raman Spectroscopy (CARS).

-

<sup>\*</sup> wright@chem.wisc.edu

Spectral fingerprints form the heart of many analytical applications because they both identify the presence of particular sample components and changes in those components. The multiple vibrational features in infrared and Raman spectra are sharp and act as fingerprints that uniquely identify specific molecules. The electronic features in UV/Visible, fluorescence excitation, and resonance Raman excitation are much broader and more intense. They provide the enhancements required to reach higher signal levels and lower detection limits. These methods are compromised when applied to complex samples like peptides and proteins because the vibrational features of individual amino acids overlap and cause spectral congestion. The inhomogeneous broadening that results from the different environments in a biological sample decreases the resolution further. The congestion and broadening prevents resolution of individual components. Coherent multidimensional spectroscopy (CMDS) is an emerging technology that provides multidimensional spectral signatures that offer selectivity advantages for the complex samples encountered in analytical chemistry applications. CMDS methods are analogous to multidimensional NMR in that they involve excitation of vibrational and electronic quantum states instead of nuclear spin states.

Multidimensional NMR avoids the spectral congestion and inhomogeneous broadening in complex samples by creating multiple quantum coherences (MQC), i.e. quantum mechanical superpositions of nuclear spin states such as those of <sup>1</sup>H and <sup>13</sup>C in different chemical environments. Pairs of states within the MQC emit signals at the frequency difference between the states. Since excitation of the MQCs in all the nuclei within the excitation region occurs by the same excitation pulse, they oscillate in phase. Unlike incoherent spectroscopies, the emission from MQCs is cooperative and coherent because the signals from different nuclei have phase relationships that constructively interfere. The selectivity of NMR is high because the spectral features are narrow and spread over multiple spectral dimensions. Even more importantly, the spin quantum states in the MQC must be coupled by interactions between the spins to create cross peaks. Coupling is a crucial factor in resolving spectral congestion because any cross-peaks between states are constrained to those associated with interactions.

Inhomogeneous broadening is another important factor in limiting spectral selectivity. A distribution of environments within a sample results in a randomization of the spin frequencies and broader spectral features. Spin echo sequences can eliminate inhomogeneous broadening using two excitation pulses. The two pulses create correlations between coherences excited by each pulse. The correlations enhance the output signal but are only present if the two coherences correspond to spins coming from the same environment within the inhomogeneous distribution.

There is another subtle reason for the NMR's high selectivity. Fully coherent spectroscopies like NMR rely on maintaining a phase relationship between all of the MQCs excited in a sample so the emission is coherent. Loss of the phase relationship by dephasing effects results in loss of the signal. Incoherent spectroscopies like fluorescence and Raman have no phase relationships between the MQCs in a sample because interactions with the environment randomizes the phases. The subsequent emission is incoherent. If an excited state population relaxes to another state, new spectral features are seen in an incoherent spectroscopy and spectral congestion increases. New features are not seen in coherent spectroscopies because population relaxation to another state destroys the phase relationships required to create spectral features. Narrow peaks, multiple dimensions, coupling,

inhomogeneous line narrowing, and fully coherent processes are all important in creating multidimensional fingerprints that uniquely identify samples as complex as proteins.

Recent work has resulted in the development of multiresonant coherent multidimensional spectroscopies (CMDS) that are based on creating MQCs of electronic and vibrational states. These spectroscopies mirror the characteristics of multidimensional NMR.1 Their origins rest in coherent Raman spectroscopy.2-7 The first example of multiresonant CMDS was fully resonant Coherent Anti-Stokes Raman Spectroscopy (CARS) where three excitation pulses with frequencies,  $\overline{v}_i$ , create a MQC of an electronic state, a vibrational state, and a vibronic state.4-8 The coupling between these states that is required for analytical applications was demonstrated using the quantum states of pentacene.9 Fig. 1a shows the three successive transitions that create a

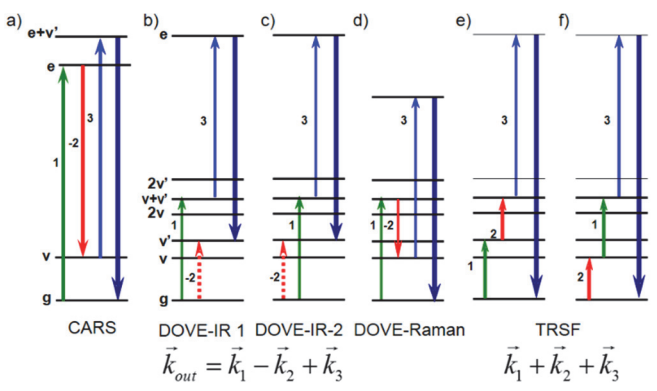


Figure 1 – Representative fully coherent four wave mixing methods. The solid and dotted arrows indicate the transitions that create the initial and final states that form the output signal, respectively. They are time-ordered from left to right with the last arrow representing the output signal. The numbers designate the excitation frequencies and the letters designate ground, vibrational, and electronic states. Solid and dashed arrows define the transitions required to reach the two states creating the output transition. a) Pathway with two successive Raman transitions connecting vibrational and vibronic states. b-d) Pathways with fundamental and combination band vibrational transitions and a Raman transition. e, f) Pathways with two successive fundamental transitions and a Raman combination band transition.

nonlinear polarization. The nonlinear polarization then creates the final output signal (final arrow in Fig. 1). The transitions are time-ordered from left to right and the solid and dotted arrows define the pathways that excite the final two states creating the nonlinear polarization. Note that the arrow direction defines the initial and final states of a transition and not whether absorption or emission occurs. In CARS and other frequency domain multiresonant CMDS methods, a spectrum is measured by scanning the frequencies of the excitation pulses and measuring the intensity of the output nonlinear polarization. Each resonance multiplicatively enhances the output signal by factors of 10<sup>3</sup>-10<sup>4</sup> above a non-resonant signal. In the CARS example, the output is formed by emission between the upper vibronic state (e+v') and the ground state (g). Unlike incoherent Raman and fluorescence spectroscopy, the output emission is coherent. cooperative, bright, and directional because the transition dipoles of the vibronic/ground state coherence have spatial and temporal phase relationships that constructively interfere in a specific direction. The direction of constructive interference is determined by the conservation of momentum between the three excitation beams and the final output beam. Momentum conservation is optimized by angling the excitation beams so the phase of the nonlinear polarization matches the phase of the output beam that it creates. 10

The spectrum measured by scanning the three input laser frequencies is three dimensional and shows the resonance enhancements with the electronic, vibrational, and vibronic states. The 3D spectra are a 3D spectral fingerprint that provides the selectivity required to study complex samples. Like IR and Raman spectroscopy, high selectivity results from the involvement of narrow vibrational and vibronic resonances. Like UV/Visible absorption and resonance Raman, the involvement of strong electronic transitions improves detection limits. The greatest challenge in implementing this methodology lies in maintaining the proper phase matching angle and the temporal and spatial overlap of the three excitation beams while

scanning the frequencies of each beam. Commercial systems do not adequately correct the pointing, and the spatial and temporal positions of the output pulses when the frequency is continuously scanned. Automated control is required to correct for the changes during a frequency scan.

The CARS method was later generalized to include different time orderings, frequencies, and phase matching conditions, that resulted in Multiresonant Non-Parametric Spectroscopy (MENS), Multiply Enhanced Parametric Spectroscopy (MEPS), and Coherent Stokes Raman Spectroscopy (CSRS). These methods are complementary and provide different capabilities. For example, although they can all narrow inhomogeneously broadened spectral features to reveal the homogeneously broadened lines hidden below, they differ in the conditions required to narrow the lines. In particular, the phases of coherences on the molecules that are non-resonant within an inhomogeneously broadened ensemble must constructively interfere with the coherences on the fully resonant molecules. The coherences formed by CARS will constructively interfere if the broadening is anti-correlated, i.e., when the broadening shifts quantum levels in opposite directions. The coherences formed by MENS will constructively interfere if the broadening is correlated, i.e., when the broadening shifts quantum levels in the same direction. These effects are discussed more completely in reference 11.

Although these coherent Raman methods used fully resonant pathways, they only involved a single vibrational ground state resonance. To involve two vibrational resonances, we extended this family of coherent resonance Raman methods to fully coherent resonance infrared absorption methods through the development of Doubly Vibrationally Enhanced (DOVE)<sup>12-18</sup> and Triply Resonant Sum Frequency (TRSF)<sup>19-21</sup> CMDS. These fully coherent pathways do not involve any intermediate populations and therefore population dynamics do not influence the spectra. They are insensitive to the bleaching, stimulated emission, and excited state absorption pathways characteristic of photon echo CMDS methods or the quenching effects of fluorescence methods. They are complementary to each other. Both create output beams that are spectrally resolved from the excitation beams so there is excellent discrimination against scattered light from the excitation beams. The TRSF pathway has particularly high spectral resolution. The DOVE pathway is particularly capable of accessing low frequency modes since the second resonance depends on the difference in excitation frequencies.

Figs. 1b-d show the resonances involved in DOVE spectroscopy. 12-14 The output transition occurs between the last two states. The solid and dotted arrows describe the transitions responsible for creating the last two states and the numbers designate the excitation frequencies. The output frequency is  $\vec{v}_{out} = \vec{v}_1 - \vec{v}_2 + \vec{v}_3$  and the direction of the output beam is defined by the phase matching or momentum conservation condition for the k vectors,  $\vec{k}_{out} = \vec{k}_1 - \vec{k}_2 + \vec{k}_3$ . The DOVE-Raman and DOVE-IR outputs have different output phases, so interference effects must be considered to understand the resulting DOVE spectra. These interference effects are important in defining the ability of different pathways to narrow inhomogeneous broadening. The DOVE-IR2 pathway narrows inhomogeneously broadened transitions between quantum states with correlated broadening while the DOVE-IR1 and DOVE-Raman pathways narrow transitions between states with anti-correlated broadening.

Fig. 1e, f shows the resonances involved in TRSF spectroscopy. <sup>19-21</sup> The two pathways differ in the time ordering of the interactions. The output frequency is  $\overline{V}_{out} = \overline{V}_1 + \overline{V}_2 + \overline{V}_3$  and the

direction of the output beam is defined by  $\vec{k}_{out} = \vec{k}_1 + \vec{k}_2 + \vec{k}_3$ . The first interaction creates a single quantum coherence while the second interaction creates a double quantum coherence. These pathways also add coherently to create the output signal. They narrow inhomogeneous broadened transitions between states with anti-correlated broadening.

DOVE and TRSF spectroscopy are very similar in the sequence of transitions that occur but they differ in the nature of the vibrational and electronic states that are accessed. Each pathway involves an overtone or combination band transition that requires coupling between the vibrational states. For molecules with a center of inversion, the two DOVE-IR pathways in Figs. 1b,c involve an *ungerade* v mode, a *gerade* v' mode, and a *ungerade* v+v' combination band. The Raman transition has *gerade* symmetry and occurs between the v+v' *ungerade* combination band and the *ungerade* v mode. The DOVE-Raman pathways in Fig. 1d involves the same v, v', and v+v' states but the final *gerade* Raman transition occurs between the *gerade* v' state and the *gerade* ground state. On the other hand, the TRSF pathway in Fig. 1e involves two transitions for v or v' *ungerade* modes to reach a *gerade* v+v' combination band. The Raman transition has *gerade* symmetry and occurs between the v+v' *gerade* combination band and the *gerade* ground state. These differences in the nature of the states makes these methods complementary to each other.

In this paper, we present the first electronically resonant DOVE CMDS spectra and compare it with TRSF CMDS spectra<sup>19</sup> using the laser dye, LDS821 (also called Styryl 9M) as a model compound. LDS821 is a convenient model because it has a strong absorption peak (molar absorptivity of 7x10<sup>4</sup> M<sup>-1</sup> cm<sup>-1</sup>) that provides an electronic resonance. The DOVE and TRSF vibrational spectra have multidimensional features at similar frequencies but there are differences that depend on the nature of the resonances and the coupling between states.

### **Experimental**

The CMDS instrument system has been described in earlier publications. 19-21 Briefly, it uses a 1 kHz Ti: sapphire regenerative amplifier to pump two optical parametric amplifiers with AgGaS<sub>2</sub> difference frequency crystals that create two independently tunable infrared beams. A third beam at 800 nm is derived from the regenerative amplifier. The wavelength dependent changes in pointing and temporal and spatial overlap of the three excitation beams is corrected by developing calibration curves that smoothly correct the changes using external mirrors and delay stages (more detailed information is available in the Supplemental Information). The three excitation beams are focused into the sample at angles to each other. They excite MQCs in the sample that cooperatively emit light at the output frequencies. Since the emission is cooperative, the output intensity scales quadratically with the sample concentration. The output beams at  $\vec{k_1} - \vec{k_2} + \vec{k_3}$  and  $\vec{k_1} + \vec{k_2} + \vec{k_3}$  are isolated and measured for the DOVE and TRSF spectra, respectively. A 800 nm notch filter rejects the 800 nm excitation beam. A photomultiplier coupled to a monochromator measures the intensity of the output beams at  $\overline{v}_1 - \overline{v}_2 + \overline{v}_3$  and  $\overline{v}_1 + \overline{v}_2 + \overline{v}_3$ , respectively. Typical values for the spectral and temporal pulse widths are ~15 cm<sup>-1</sup> and ~1.2 ps FWHM, respectively. Two-dimensional spectra result from scanning  $\overline{v}_1$  and  $\overline{v}_2$  and measuring the output beam intensity. Typically, complete spectra require ~2.5 hours. In order to eliminate the quadratic dependence on sample concentration, the spectral intensities are converted to amplitudes by taking the square root of the signal intensity. This conversion allows direct comparison of the relative intensities with IR and Raman spectra. Finally, the time delays between pulses change as the frequencies are scanned. In order to

eliminate these changes, the system has been automated to correct the time delays during spectral scans.

The sample for this work was 2-(6-(p-dimethylaminophenyl)-2,4-neopentylene-1,3,5hexatrienyl)-3-ethylbenzothiazolium perchlorate (Styryl 9M or LDS821).<sup>22</sup> The sample concentration was 300 µM in deuterated acetonitrile. The sample also contained 180 mM benzene as an absorption spectrum standard. The sample cell path length was 25 µm.

## **Theory**

Treatment of the theoretical description of multiresonant CMDS follows that given in earlier publications. 5, 11, 23-24 The spatial and temporal dependence of the total electric field from the three excitation pulses is

$$\vec{E} = \sum_{i=1}^{3} E_{i}^{o}(t) \left( e^{i\left(\vec{k}_{i} \cdot \vec{z} - \omega_{i}t\right)} + e^{-i\left(\vec{k}_{i} \cdot \vec{z} - \omega_{i}t\right)} \right)$$

$$\tag{1}$$

where  $\vec{k}_i \cdot \vec{z}$  is the wave vector in the propagation direction,  $\vec{z}_i$ ,  $\omega_i = 2\pi c \vec{v}_i$  is the angular frequency, and  $E_{i}^{o}\left(t
ight)$  is the slowly varying amplitude of the pulse envelope of the  $\emph{i}^{th}$  excitation

beam, typically of the form  $e^{-(t-\tau)^2/\sigma^2}$  . The electric field creates a nonlinear polarization which, in the frequency domain, is given by  $\vec{P}_{NL}=\chi^{(3)}\vec{E}^3$  where  $\chi^{(3)}$  is the third order susceptibility tensor. The third order nonlinear polarization then has many cross terms that depend on the number of interactions,  $n_i$ , with each  $i^{th}$  field. A typical cross-term for the nonlinear polarization amplitude is given by

where 
$$\sum_{i=1}^{3} n_i = 3$$
. For DOVE spectroscopy,  $n_i = 1$ ,  $k_{NL} = k_1 - k_2 + k_3$ , and  $\omega_{NL} = \omega_1 - \omega_2 + \omega_3$ .

Similarly, for TRSF spectroscopy,  $\vec{k}_{NL} = \vec{k}_1 + \vec{k}_2 + \vec{k}_3$  and  $\omega_{NL} = \omega_1 + \omega_2 + \omega_3$ . The spatially and temporally oscillating nonlinear polarization creates the output field amplitudes,  $E_{out}^o$ , through the relationship

$$\frac{\partial E_{out}^{o}}{\partial z} + \frac{n}{c} \frac{\partial E_{out}^{o}}{\partial t} = \frac{2\pi i F \omega P_{NL}^{o}}{nc} e^{i\Delta kz}$$
(3)

where c is the speed of light,  $\Delta \vec{k} \equiv \vec{k}_{out} - \vec{k}_{NL}$  , and n is the refractive index. Ideally,  $\Delta k$  is zero so the wavelength of the output beam phase matches the nonlinear polarization that created the beam. Constructive interference then occurs throughout the excitation volume and the emission is coherent. The excitation beams are angled to optimize this phase matching along the propagation direction of the output beam. The magnitude of a wave vector is  $k = \frac{n\omega}{a}$ . In the case of normal dispersion, TRSF cannot be phase matched because the k-vector of the output

beam is longer than the sum of the nonlinear polarization k-vectors. The effects are small if the excitation path length is short,  $\Delta \vec{k} l << 1$ .

The output transition for the DOVE process in Figs. 1b, c occurs between states e and v. The sequence of transitions required to reach those states is defined by Liouville pathways  $gg \xrightarrow{1} v + v', g \xrightarrow{2} v + v', v \xrightarrow{3} ev \text{ and } gg \xrightarrow{2} gv \xrightarrow{1} v + v', v \xrightarrow{3} ev$ . The label for the excitation pulse arrows define the frequencies, not the time ordering, and carry the sign of the wave vector that defines whether the transition involves absorption or emission. The mn letters define the states involved in the mn coherences required to reach the output transition where g is the ground state, v and v' are vibrational states, v+v' is a combination band, and e is an electronic state. The output transition for Fig. 1d occurs between states e and e so the pathway is  $gg \xrightarrow{1} v + v', g \xrightarrow{2} vg \xrightarrow{3} eg$ . The nonlinear polarizations created by each of these paths are coherent and interfere. The e values for each pathway are therefore additive. In the steady state approximation where the excitation is long compared with the dephasing time, the third order susceptibility is the sum of the contributions from the three pathways:

$$\chi^{(3)} = \frac{NF}{4D\hbar^3} \left( -\frac{\mu_{g,\nu+\nu'}\mu_{g\nu}\mu_{\nu+\nu',e}\mu_{e\nu}}{\Delta_{\nu+\nu',g}^1\Delta_{\nu+\nu',\nu}^{1-2+3}} - \frac{\mu_{g\nu}\mu_{g,\nu+\nu'}\mu_{\nu+\nu',e}\mu_{e\nu}}{\Delta_{g\nu}^{-2}\Delta_{\nu+\nu',\nu}^{1-2+3}} + \frac{\mu_{g,\nu+\nu'}\mu_{\nu+\nu',\nu}\mu_{\nu'e}\mu_{eg}}{\Delta_{\nu+\nu',g}^1\Delta_{\nu'g}^{1-2+3}} \right)$$
(4)

where N is the concentration, F is a field enhancement factor, D is a degeneracy factor that is six for the Maker-Terhune convention<sup>25</sup>, the  $\mu_{mn}$  are the transition moments for the  $m\rightarrow n$  transition,  $\Delta_{mn}^{excit}=\omega_{mn}-\omega_{excit}-i\Gamma_{mn}$  are the resonance factors for the mn coherence,  $\omega_{mn}$  and  $\Gamma_{mn}$  are the frequencies and dephasing rates of the mn coherence, respectively, and excit represents the resonant excitation frequencies (eg. excit =1-2 represents  $\omega_1-\omega_2$ ). The resonance factors in Eqn. 4 define the Lorentzian line shape and center frequency of each transition. The first and last terms have opposite signs but similar transitions so they destructively interfere. Note that the  $\mu_{g,v+v'}$  transition moment describes a forbidden combination band (or overtone if v=v') that requires mechanical and/or electrical anharmonicity<sup>26</sup> and that the  $\mu_{v+v',e}$  and  $\mu_{ev}$  transition moments are associated with a resonance Raman transition involving v while v' remains unchanged.

The output transition for the TRSF processes in Figs. 1e,f occurs between states e and g. The Liouville pathways are  $gg \xrightarrow{1} vg \xrightarrow{2} v + v', g \xrightarrow{3} eg$  and  $gg \xrightarrow{2} vg \xrightarrow{1} v + v', g \xrightarrow{3} eg$ . The third order susceptibility is

$$\chi^{(3)} = \frac{NF}{4D\hbar^3} \left( \frac{\mu_{gv} \mu_{v,v+v'} \mu_{v+v',e} \mu_{eg}}{\Delta_{vg}^1 \Delta_{v+v',g}^1 \Delta_{eg}^{1+2+3}} + \frac{\mu_{gv} \mu_{v,v+v'} \mu_{v+v',e} \mu_{eg}}{\Delta_{vg}^2 \Delta_{v+v',g}^{1+2+3}} \right). \tag{5}$$

Note that the  $\mu_{g,v}$  and  $\mu_{v,v+v'}$  transition moments are allowed fundamental vibrational transitions while the  $\mu_{v+v',e}$   $\mu_{eg}$  resonance Raman transition moments is a combination band (or overtone) transition that requires coupling between the electronic state and both v and v'.

The steady state approximation used here assumes the excitation pulses temporal widths are long compared to the dephasing time so the molecular response is driven by the excitation fields. If the pulses are short compared to the dephasing time, the molecular response is defined by the free induction decay of the coherences. In this work, the excitation pulse width is comparable to the vibrational dephasing time so the output signal has both driven and free induction decay components. The treatment for this intermediate case is described in a separate publication.<sup>27</sup> In this paper, we assume the steady state limit.

### **Results and Discussion**

Figure 2 shows the two dimensional TRSF spectrum of Styryl 9M.<sup>19</sup> The  $\overline{\nu}_1$  and  $\overline{\nu}_2$  pulses were temporally overlapped so either pulse can create the first or second interaction. Both frequencies were scanned over a 1250-1600 cm<sup>-1</sup> range while  $\overline{\nu}_3$  was fixed at 12,500 cm<sup>-1</sup>. The sum of the three frequencies ranged from 15,000-15,700 cm<sup>-1</sup>. Monochromator scans show that the output frequency always occurs at  $\overline{\nu}_1 + \overline{\nu}_2 + \overline{\nu}_3$  as expected for a driven signal. The maximum electronic resonance enhancement is expected when  $\overline{\nu}_{eq}$  is equal to  $\overline{\nu}_1 + \overline{\nu}_2 + \overline{\nu}_3$  since the

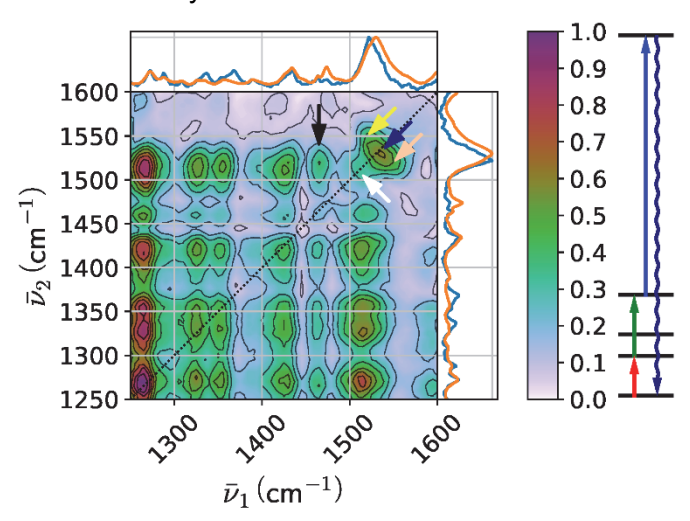


Figure 2-TRSF spectrum of Styryl 9M dye. The x and y axes define the excitation frequencies and the color bar defines the output amplitude. The dotted line defines the overtone feature positions. The Raman (orange) and IR absorption (blue) appear above. The coherence pathway on the right is shown for reference.

electronic state transition occurs from the overtone or combination band state. This frequency range is resonant with the red side of the electronic transition that occurs at 17,700 cm<sup>-1</sup> with a 3350 cm<sup>-1</sup> HWHM. The electronic resonance enhancement results in very strong TRSF output signals even though the Styryl 9M concentration is too low to measure infrared spectra. Other experiments showed that neither deuterated acetonitrile nor benzene solvent peaks appear under the conditions of these experiments since they lack either suitable vibrational or electronic resonances. Fig. 2 also shows the infrared solvent subtracted absorption spectrum taken at much higher concentrations (blue trace) and the resonance Raman spectrum (orange trace). Note the strong similarity between the IR absorption and resonance Raman spectra. The two spectra are almost identical because this molecule lacks symmetry so both Raman and infrared absorption transitions are allowed for each vibration. The TRSF spectrum contains diagonal peaks where the interactions create fundamental and overtone transitions with low anharmonicity and cross-peaks where the interactions create fundamental and combination band transitions for all of the vibrational transitions observed in the resonance Raman and infrared spectra, except for the diagonal feature at 1530 cm<sup>-1</sup> that lacks cross-peaks. The presence of so many cross-peaks shows there is strong vibrational-electronic coupling between states. Strong coupling might be expected because Styryl 9M is extensively conjugated so the electronic states are strongly affected by vibrational motions.

There are two features in the spectra that merit further discussion. The peak at  $(\overline{\nu}_1, \overline{\nu}_2)$  = (1512, 1512) cm<sup>-1</sup> (white arrow) is the diagonal peak for a fundamental vibrational mode but the

peak at (1530, 1530) (blue arrow in Fig. 2) has an anti-diagonal shape when  $\overline{\nu_1}$  and  $\overline{\nu_2}$  are temporally overlapped. If a delay is created between the first two interactions so the  $\overline{\nu_1}$  pulse precedes the  $\overline{\nu_2}$  pulse, the peak resolves into two peaks at  $(\overline{\nu_1}, \overline{\nu_2}) = (1512, 1545)$  cm<sup>-1</sup> (yellow arrow in Fig. 2) and (1531, 1527) cm<sup>-1</sup> (near blue arrow). For the (1512, 1545) cm<sup>-1</sup> peak,  $\overline{\nu_1}$  excites the fundamental mode at 1512 cm<sup>-1</sup> and  $\overline{\nu_2}$  excites a Fermi resonance with a state at 3057 cm<sup>-1</sup>. The latter state cannot be seen in infrared and Raman spectra because it is obscured by strong C-H resonances. For the (1531, 1527) cm<sup>-1</sup> peak,  $\overline{\nu_1}$  excites a fundamental mode at 1531 cm<sup>-1</sup> and  $\overline{\nu_2}$  excites the overtone of the same mode but it also has a Fermi resonance with the same state at 3057 cm<sup>-1</sup>. The 1531 cm<sup>-1</sup> is obscured by the 1512 cm<sup>-1</sup> mode in the infrared spectrum and may be responsible for the unresolved and asymmetric line shape in the resonance Raman spectrum. The absence of cross-peaks for the 1531 cm<sup>-1</sup> mode may indicate that those cross-peaks either do not have the same Fermi resonance and/or that the mode is not coupled to the other modes in the spectrum. Similarly, if the  $\overline{\nu_2}$  pulse precedes the  $\overline{\nu_1}$  pulse, peaks will appear at (1545, 1512) (tan arrow) and (1527, 1531) cm<sup>-1</sup>. Together, they create the anti-diagonal feature at  $(\overline{\nu_1}, \overline{\nu_2}) = (1530, 1530)$  in Fig. 2.

The second feature in the spectrum are the series of diagonal and cross-peaks associated with features at 1467 cm<sup>-1</sup> (black arrow in Fig. 2). Two peaks appear as a 9 cm<sup>-1</sup> doublet at 1467 cm<sup>-1</sup> in the infrared and resonance Raman spectra. The spacing is narrower than the 15 cm<sup>-1</sup> excitation pulse bandwidth so both resonances are excited with the excitation pulse. They appear as a single peak in Fig. 2 but they split in spectra taken at different time delays. The splitting is a manifestation of frequency domain quantum beating. The beating appears in TRSF spectra as a periodic splitting with a 3.7 ps period into two features as a function of the time delay between the first two excitation pulses. The period corresponds to the frequency difference between the two states.<sup>19</sup>

Figure 3 shows the two-dimensional DOVE spectrum of Styryl 9M along with the resonance Raman and infrared absorption spectra. The dotted line is the 'overtone line,' where  $\overline{\nu}_1=2\overline{\nu}_2$ . We expect overtone peaks with very small anharmonicity to appear on this line. The  $\overline{\nu}_1$  pulse was delayed by 1 ps from the  $\overline{\nu}_2$  pulse while the  $\overline{\nu}_3$  pulse was delayed by 2 ps from the  $\overline{\nu}_1$  pulse. These delay times isolate the DOVE IR2 pathway in Fig. 1c and avoid destructive interference effects from the DOVE IR1 and DOVE Raman pathways. The  $\overline{\nu}_1$  and  $\overline{\nu}_2$  frequencies were scanned over the 1250-1550 and 2500-3100 cm-1 range, respectively, while  $\overline{\nu}_3$  was fixed at 12,500 cm-1. The output frequency at  $\overline{\nu}_{out}=\overline{\nu}_1-\overline{\nu}_2+\overline{\nu}_3$  then ranged from 13,450-14,350 cm-1. The peak electronic resonance for the DOVE-IR and DOVE-Raman pathways are substantially different. In DOVE-IR, the transition to the electronic state is from the combination band or overtone state excited by  $\overline{\nu}_1$ , giving maximum resonance when  $\overline{\nu}_{eg}=\overline{\nu}_1+\overline{\nu}_3$ . Conversely, the transition to the electronic state in the DOVE-Raman pathway

starts from a vibrational state with the energy  $\overline{v}_1 - \overline{v}_2$  so the electronic resonance is maximized when  $\overline{\nu}_{\rm \tiny \it eg} = \overline{\nu}_{\rm \tiny \it l} - \overline{\nu}_{\rm \tiny \it \it l} + \overline{\nu}_{\rm \tiny \it \it \it \it l}$  . Because the DOVE-IR electronic resonance was already on the red side of the electronic state, the DOVE-Raman pathway is largely not resonant with the electronic state and is not expected to contribute substantially to the spectrum. Regardless of the electronic resonance criteria, the output frequency always occurs at  $\overline{V}_1 - \overline{V}_2 + \overline{V}_3$ , as predicted by the phase matching and verified by monochromator scans. The spectrum has similar resonances to all those in the TRSF spectrum although the relative intensities may differ. The relative intensities of the features cannot be quantitatively compared because of uncertainties in the changes in temporal delay times during the spectral scans. Both types of spectra resolve a background between vibrational features. The background has vertical and diagonal symmetry in the DOVE spectrum and vertical and horizontal symmetry in the

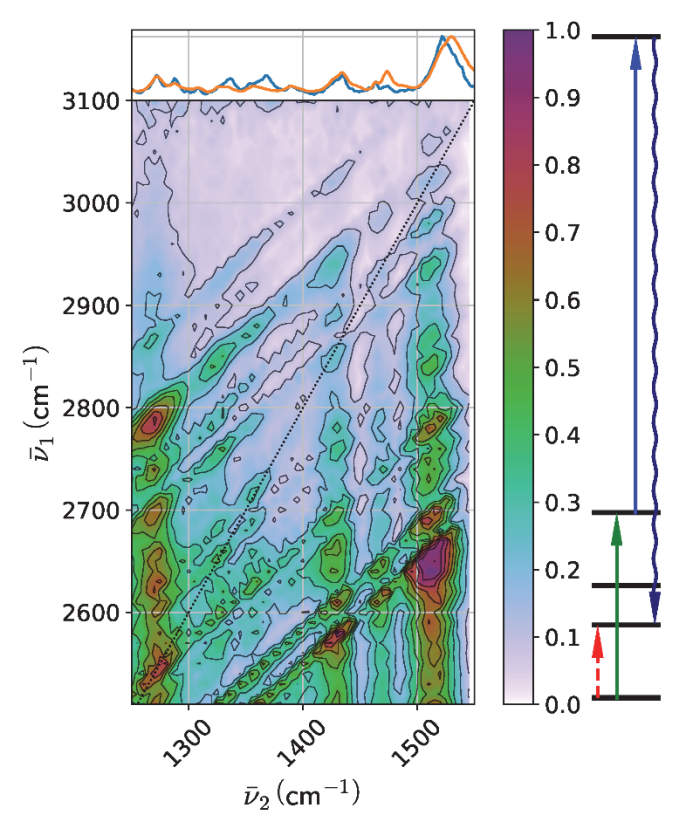


Figure 3- DOVE spectrum of Styryl 9M dye. The axes define the two excitation frequencies and the color bar defines the output amplitude. The dotted line defines the overtone feature positions. The resonance Raman (orange) and IR absorption (blue) spectra appear above. The coherence pathway on the right is shown for reference.

TRSF spectrum. The nature of this background requires further research. Many vibrational features in infrared absorption and Raman spectra include an underlying background signal. The symmetry associated with the DOVE and TRSF spectra is consistent with line narrowing of an inhomogeneously broadened ensemble.

The vertical and diagonal character of the DOVE-IR2 spectral features results from the nature of the vibrational resonant enhancements. The dominant factors in Eqn. 4 for the DOVE-IR2 pathway are  $\Delta_{gv}^{-2}\Delta_{v+v',v}^{1-2}$ . The  $\Delta_{gv}^{-2}$  resonance is responsible for the vertical character of the resonances while the  $\Delta_{v+v',v}^{1-2}$  is responsible for the diagonal character. In order to provide a better comparison of the spectra, the DOVE spectrum can be modified with the ordinate changed to  $(\overline{v_1}-\overline{v_2})$  such that the y-axis represents v rather than v+v' for better comparison to the TRSF spectrum in Fig 4. The spectral features are similar but there are differences. The diagonal peak at (1512, 1512) cm-1 appears in both spectra but the anti-diagonal feature in the TRSF spectrum is missing in the DOVE-IR2 spectrum.

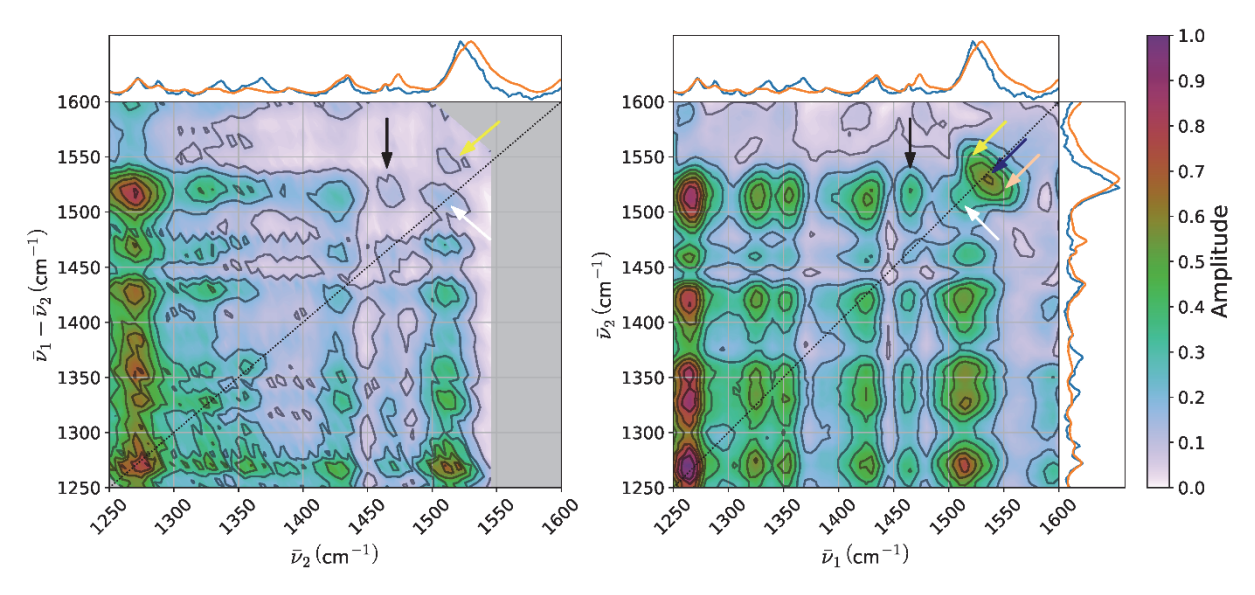


Figure 4-The Styryl 9M dye DOVE and TRSF spectra are compared by redefining the DOVE spectrum y-axis from  $\overline{V}_1$  to  $\overline{V}_1 - \overline{V}_2$  The dotted line defines the overtone feature positions.

Fig. 5 shows the same spectrum as Fig. 3 except the ordinate range has been expanded in order to demonstrate the second difference- the ability to observe coupling to lower frequency vibrational modes using the  $(\overline{\nu_1} - \overline{\nu_2})$  difference frequency. The interaction with  $\overline{\nu_2}$  defines the initial mode, v', while the interaction with  $\overline{\nu_1}$  defines the combination band involving that mode, i.e. v+v' where v' may be a low frequency mode. The capability for probing low frequency modes is similar to Raman methods but in this case, the  $\omega_1$  induced transition is an IR absorption. The figure shows the correspondence between the 2D cross-peaks below 1250 cm<sup>-1</sup> that correspond to similar features in both the infrared absorption and resonance Raman transitions.

The third difference arises in comparing DOVE spectrum with the anti-diagonal TRSF feature in Fig. 2 at  $(\overline{\nu}_1,\overline{\nu}_2)$  = (1530, 1530) cm<sup>-1</sup>. That TRSF feature was resolved into two peaks at  $(\overline{\nu}_1,\overline{\nu}_2)$  = (1512, 1545) and (1531, 1527) cm<sup>-1</sup>. The peaks were ascribed to a Fermi resonance of the 1512 cm<sup>-1</sup> mode with a state at 3057 cm<sup>-1</sup> and a diagonal peak at  $\overline{\nu}_1-\overline{\nu}_2$  = 1531 cm<sup>-1</sup> which was also enhanced because it shared the same Fermi resonant state. Comparing TRSF and DOVE spectra, there is a weak feature in the DOVE spectrum at  $(\overline{\nu}_2,\overline{\nu}_1-\overline{\nu}_2)$  = (1511, 1545) [or  $(\overline{\nu}_2,\overline{\nu}_1)$  = (1511, 3056) cm<sup>-1</sup>] that corresponds to the TRSF feature and is consistent with the Fermi resonance assignment. There is also a weak feature in the DOVE spectrum near  $(\overline{\nu}_2,\overline{\nu}_1-\overline{\nu}_2)$  = (1511, 1508) cm<sup>-1</sup> [or  $(\overline{\nu}_2,\overline{\nu}_1)$  = (1511, 3019) cm<sup>-1</sup>] that corresponds to the diagonal TRSF feature at  $(\overline{\nu}_1,\overline{\nu}_2)$  = (1512, 1510) cm<sup>-1</sup>. The presence of these features provides additional evidence for the role of the Fermi resonant state at 3057 cm<sup>-1</sup>.

### **Conclusions**

Just as multidimensional NMR has become a standard method for protein characterization, CMDS methods offer the promise of extending coherent methodology to the complex samples encountered by analytical chemists. Meeting this promise requires the participation of the analytical research community. Together with the other Raman based methods, DOVE and TRSF CMDS complete the fully coherent family of methods that are analogues to the incoherent spectroscopies that dominate analytical measurements such as infrared, UV/Visible absorption and fluorescence methods. 1, 28 All are based on exciting vibrational and/or electronic states. They differ because incoherent methods create excited state populations that undergo relaxation while fully coherent spectroscopies create quantum mechanical superposition states that undergo dephasing. Although relaxation processes contribute to the dephasing, they only control the homogeneous line width of spectral features and do not create new features resulting from population relaxation.

There are a number of characteristics that these fully coherent CMDS methods offer for analytical spectroscopy. First, is their ability to create multidimensional spectral signatures of vibrational and electronic states characteristic of specific molecules and materials. The selectivity acquired from multidimensional signatures is particularly important for probing complex materials where spectral congestion and line broadening limit the use of conventional spectroscopic methods. Spectral congestion is resolved because the

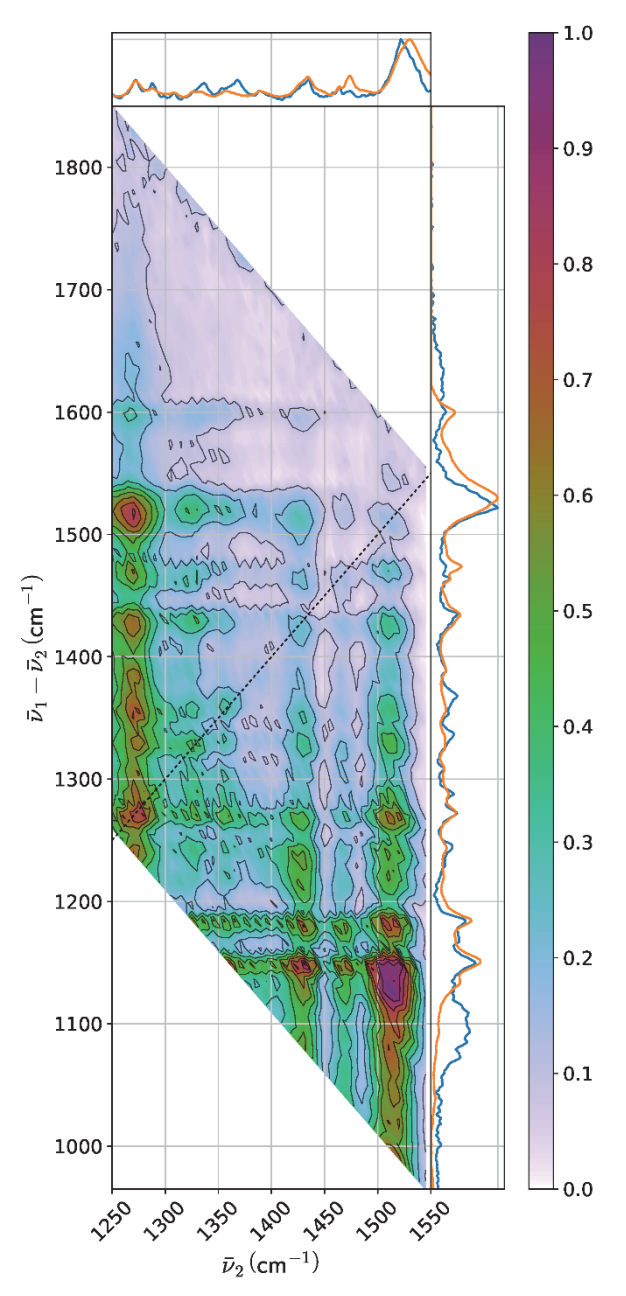


Figure 5--- Expanded view of the DOVE spectrum of Styryl 9M dye to show the low frequency vibrational features. The y-axis is  $\overline{V}_1 - \overline{V}_2$ . The dotted black line defines the diagonal feature positions.

spectral features are spread over multiple dimensions and because the only cross-peaks that appear are those arising between states that are coupled. Inhomogeneously broadened spectral features can be narrowed using CMDS pathways that selectively excite multiple transitions from fully resonant molecules within an inhomogeneously broadened ensemble. The fully coherent CMDS pathways lessen spectral congestion resulting from the creation of new cross-peaks from population relaxation processes. They create output beams that are spectrally resolved from the excitation beams so discrimination against scattered excitation light

is excellent. Both CARS and DOVE pathways depend on the frequency differences between excitation pulses so low frequency vibrational modes can be accessed.

A recent publication discusses the future directions of using higher order CMDS for analytical applications.<sup>1</sup> These higher order applications would be analogous to multidimensional NMR involving more than three excitation pulses. The DOVE and TRSF methods described here involve three nonlinear interactions that create an output signal. However, these methods can also be extended to higher order processes involving an arbitrary number of interactions with excitation beams. We consider two particularly promising applications. The first is pump-CMDS probe. Fully coherent CMDS methods like DOVE, TRSF, and CARS do not involve intermediate populations so population relaxation does not affect the spectra. These signals arise from direct coupling between states during the time of the lightmatter interactions. A pump-CMDS probe experiment therefore isolates the population dynamics to the time delay between the pump and multidimensional probe pulses. This method of probing dynamics would be particularly useful for complex materials.

The second involves multiple interactions with each excitation beam. Experiments have shown the feasibility of having 11 interactions that excite vibrational ladders of overtone and combination band coherences up to the fifth overtone state.<sup>29-30</sup> Such energetic overtones and combination band states are near the dissociation limit and therefore serve as excellent probes of the multidimensional molecular potential energy surface. This approach will become increasingly powerful as methods for controlling the pulse shape evolve so excitation frequencies change on a femtosecond time scale to match the anharmonicities that accumulate higher in a vibrational ladder.

Like multidimensional NMR, fully coherent methods can be performed in the time or frequency domain. In NMR, the time domain became the standard approach because of its multiplex advantage and because the excitation band width covered the entire range of useful frequencies. Likewise, time domain methods have dominated the field of CMDS but these methods are currently constrained because the excitation band width does not cover the entire range of useful wavelengths. There are also stringent requirements on the long term phase stability of heterodyning with a local oscillator when fully coherent methods are employed. Frequency domain methods such as those described in this work do not involve heterodyning. They require only short term phase coherence during the creation of the MQCs. As this paper shows, they can be used over the entire range of available vibrational and electronic frequencies.

**Acknowledgements**- We are indebted to Erin S. Boyle's work on this research. We also acknowledge Blaise Thompson for his extensive work on the WrightTools software package. This work was supported by the National Science Foundation under grants CHE-1410510 and CHE-1709060.

## **Supporting Information-**

- Details on the experimental methods and their corrections for beam pointing and position, temporal and spatial overlap, and phase matching changes during spectral scanning of the excitation frequencies.
- Zip file containing original data for the FTIR, Raman, and TRSF 2D spectra as well as the Python code used to graph the spectra.

#### References

- 1. Wright, J. C., Chem Phys Lett 2016, 662, 1-13.
- 2. Tolles, W. M.; Nibler, J. W.; McDonald, J. R.; Harvey, A. B., *Appl Spectrosc* **1977**, *31*, 253-271.
- 3. Druet, S. A. J.; Taran, J. P. E.; Borde, C. J., J. Phys. (Paris) 1979, 40, 819-840.
- 4. DeCola, P. L.; Andrews, J. R.; Hochstrasser, R. M.; Trommsdorff, H. P., *J Chem Phys* **1980**, *73*, 4695-4696.
- 5. Oudar, J. L.; Shen, Y. R., *Phys Rev A* **1980**, *22*, 1141.
- 6. Chang, T. C.; Johnson, C. K.; Small, G. J., J Phys Chem 1985, 89, 2984-2992.
- 7. Lee, S. H.; Steehler, J. K.; Nguyen, D. C.; Wright, J. C., *Appl Spectrosc* **1985**, 39, 243-253.
- 8. Carlson, R. J.; Nguyen, D. C.; Wright, J. C., *J Chem Phys* **1990**, 92, 1538-1546.
- 9. Carlson, R. J.; Wright, J. C., Anal Chem 1991, 63, 1449-1451.
- 10. Eckbreth, A. C., Appl Phys Lett 1978, 32, 421-423.
- Wright, J. C.; Carlson, R. J.; Hurst, G. B.; Steehler, J. K.; Riebe, M. T.; Price, B. B.;
   Nguyen, D. C.; Lee, S. H., *Int Rev Phys Chem* 1991, 10, 349-390.
- 12. Zhao, W.; Wright, J. C., *Phys Rev Lett* **1999**, 83, 1950-1953.
- 13. Zhao, W.; Wright, J. C., *J Am Chem Soc* **1999**, *121*, 10994-10998.
- 14. Zhao, W.; Wright, J. C., Phys Rev Lett **2000**, 84, 1411-1414.
- 15. Fournier, F.; Gardner, E. M.; Kedra, D. A.; Donaldson, P. M.; Guo, R.; Butcher, S. A.; Gould, I. R.; Willison, K. R.; Klug, D. R., *P Natl Acad Sci USA* **2008**, *105*, 15352-15357.
- 16. Fournier, F.; Gardner, E. M.; Guo, R.; Donaldson, P. M.; Barter, L. M. C.; Palmer, D. J.; Barnett, C. J.; Willison, K. R.; Gould, I. R.; Klug, D. R., *Anal Biochem* **2008**, *374*, 358-365.
- 17. Donaldson, P. M.; Guo, R.; Fournier, F.; Gardner, E. M.; Gould, I. R.; Klug, D. R., *Chem Phys* **2008**, *350*, 201-211.
- Donaldson, P. M.; Guo, R.; Fournier, F.; Gardner, E. M.; Barter, L. M. C.; Barnett, C. J.; Gould, I. R.; Klug, D. R.; Palmer, D. J.; Willison, K. R., *J Chem Phys* 2007, 127, 114513(1-10).
- 19. Boyle, E. S.; Neff-Mallon, N. A.; Wright, J. C., J Phys Chem A 2013, 117, 12401-12408.
- 20. Boyle, E. S.; Pakoulev, A. V.; Wright, J. C., J Phys Chem A 2013, 117, 5578-5588.
- 21. Boyle, E. S.; Neff-Mallon, N. A.; Handali, J. D.; Wright, J. C., *J Phys Chem A* **2014**, *118*, 3112-3119.
- 22. Purchased from Exciton.
- 23. Wright, J. C., Int. Rev. Phys. Chem. 2002, 21, 185-255.
- 24. Yee, T. K.; Gustafson, T. K., *Phys Rev* **1977**, *18*, 1597-1617.

- 25. Maker, P. D.; Terhune, R. W., *Phys Rev* **1965**, *137*, A801-A818.
- 26. Kwak, K.; Cha, S.; Cho, M. H.; Wright, J. C., J Chem Phys 2002, 117, 5675-5687.
- 27. Kohler, D. D.; Thompson, B. J.; Wright, J. C., *J Chem Phys* **2017**, *147*, 084202-084219.
- 28. Wright, J. C., Annu Rev Anal Chem 2017, 10, 45-70.
- 29. Mathew, N. A.; Block, S. B.; Yurs, L. A.; Kornau, K. M.; Pakoulev, A. V.; Wright, J. C., *J Phys Chem A* **2009**, *113*, 13562–13569.
- 30. Mathew, N. A.; Yurs, L. A.; Block, S. B.; Pakoulev, A. V.; Kornau, K. M.; Sibert, E. L.; Wright, J. C., *J Phys Chem A* **2010**, *114*, 817-832.